Quenching one-dimensional Rydberg atom arrays

Oliver Lind

Level 4 Project, MSci Maths and Physics

Supervisor: Professor Stuart Adams

Department of Physics, Durham University

Submitted: April 15, 2024

Quenching a quantum many-body system involves rapidly changing the parameters of the Hamiltonian such that the system is propelled out-of-equilibrium. In this work, numerical simulations of a one-dimensional Rydberg atom array quantum simulator are carried out on 7 to 9 atoms to study the out-of-equilibrium phenomena resulting from quenches. By globally quenching the system, we introduce quantum many-body scaring behaviour, characterised by the surprising revivals of the initial state. It is demonstrated that this behaviour is associated with slow entanglement entropy growth and ordered spreading of the state vector across the quenched eigenenergy spectrum. Furthermore, we perform local quenches to demonstrate a range of quantum transport phenomena concerned with the spreading of information and entanglement throughout the array. In particular, we find quasiparticle-like behaviour associated with quench on the boundary of the Rydberg anti-blockade condition. Overall, these results showcase the potential of the Rydberg atom array quantum simulator as a gateway to studying out-of-equilibrium dynamics of isolated quantum many-body quantum systems.

Contents

prepost

1. INTRODUCTION

Consider an ideal gas enclosed in a box with adiabatic walls, such that no heat is transferred outwards, and the classical system is truly closed. Imagine the box is then violently shaken for a short instance, imparting an energy E on the gas and taking the system out of equilibrium. Classical statistical mechanics tells us that, due to the chaotic motion of all particles, after a sufficient amount of time, the system will thermalise to an equilibrium state characterised by its new energy. In fact, the manner in which the box is shaken does not matter, as long as the energy imparted on the system is exactly E, the system will eventually return to the same equilibrium state.

Now, one might ask if the same applies in a closed quantum system. In quantum mechanics, time evolution is unitary and linear [1]. As a result, the evolution of the state of the system cannot be chaotic. In contrast, in the classical system, chaos enables the state to explore the entire phase space ergodically, leading to a final equilibrium state [2]. The lack of this explicit chaos in closed quantum systems means they cannot thermalise in the same way [3]. This diversion in behaviour, is one of the main reasons why studying the out-of-equilibrium dynamics of closed quantum many-body systems has drawn a lot of interest [4].

The perfect workbench to studying this phenomenon is a quantum simulator. Recently, due to advances in optical tweezers technologies, trapped ultracold neutral atom arrays have emerged as a favourite [5]. In particular, arrays consisting of Rydberg atoms: atoms with a single outer electron in a highly excited state such that the atom appears hydrogen-like. The large dipole moments of Rydberg atoms lead to strong interaction between Rydberg states [6]. Given the precision of optical tweezers, these interactions can be fine tuned, resulting in a programmable closed quantum system.

In Ref. [7], such a system was set up on a one-dimensional array of 51 neutral Rubidium atoms and the dynamics where studied. Notably, they found that quenching the system resulted in interesting out of equilibrium dynamics which challenge notions of quantum thermalisation [8]. Motivated by this result, we study different ways in which the one-dimensional Rydberg atom array can be quenched. We achieved this through numerical simulations of a scaled down version of the simulator used in Ref. [7] (See Appendix A for code).

In this report we will demonstrate that quenching the Rydberg atom array serves as an effective gateway for exploring the out-of-equilibrium dynamics of isolated quantum many-body systems and that within this regime there is a lot of rich interesting physics to be explored. The structure of the report will follow:

1. Introduce the Rydberg *qubits* and the interaction *Hamiltonian*.

2. Adiabatically evolve the Hamiltonian to generate spatially *ordered states* to be quenched.

3. Introduce *measures of entanglement* for the study of the post-quench dynamics.

4. Globally quench ordered states to introduce *quantum many body scaring* and study its underlying features.

5. Locally quench ordered states to study *quantum transport phenomena* associated with the propagation of information and entanglement.

2. BACKGROUND

In this section, we will set out the equations which can model the dynamics of the Rydberg atom array simulator, namely the Hamiltonian of the system. We will then describe how the system is evolved by varying the laser frequency incident on each of the atoms. Accordingly, we will further describe how the interactions between Rydberg states can be leveraged to evolve the system into spatially ordered states, Z_n.

When we begin quenching the array, our focus will narrow to a specific ordered state, the Z_2 state. Consequently, understanding its emergence through the system's interactions will be invaluable for uncovering the underlying dynamics.

A. Building up the Hamiltonian

1. Rydberg qubits

In Ref. [7], neutral ^{87}Rb atoms are cooled and trapped using optical tweezers into a 1D array of uniform separation. Separate orthogonal lasers are then used to couple the ground, $|0\rangle = |5S_{1/2}\rangle$, and Rydberg excited state, $|r\rangle = |70S_{1/2}\rangle$, of each atom homogeneously (see Figure 1). The coupling between the two states generates our qubit:

$$|\psi\rangle = a\,|0\rangle + b\,|r\rangle\,, \quad |a|^2 + |b|^2 = 1, \quad a, b \in \mathbb{C}. \tag{1}$$

The atomic light interaction of the two level system can be characterized by the Rabi frequency Ω, the detuning Δ, and the phase ϕ_L. The Rabi frequency is proportional to the amplitude of the driving laser field and quantifies the strength of the coupling between the two qubit states. The detuning then measures the deviation of the driving laser frequency and the qubit's resonant transition frequency. Finally the phase term ϕ_L, encodes the relative phase between the field and the qubit. Altogether, the interaction between field and qubit can be described by the following Hamiltonian:

$$\frac{H_{int}}{\hbar} = \frac{\Omega e^{-i\phi}}{2}\,|0\rangle\langle r| + \frac{\Omega e^{i\phi}}{2}\,|r\rangle\langle 0| - \Delta\,|r\rangle\langle r|\,. \tag{2}$$

For the purposes of our simulations, we are only concerned with projective measurements of the qubits in the z-axis (between the $|0\rangle$ and $|r\rangle$ states). Hence, the relative phase between field and qubit is not relevant and can be set to zero, $\phi_L = 0$. In contrast, if the qubits were used to simulate digital quantum gates, the phase term would be essential. By setting $\phi_L = 0$, the single qubit interaction Hamiltonian then becomes:

$$\frac{H_{int}}{\hbar} = \frac{\Omega}{2}(|0\rangle\langle r| + |r\rangle\langle 0|) - \Delta\,|r\rangle\langle r|\,. \tag{3}$$

To represent the Rydberg atom array platform, we need to consider N qubits coupled to the laser field in this way. If the qubits are non-interacting, we could write the Hamiltonian as follows:

$$H_{seperable} = H_{int,1} \otimes H_{int,2} \otimes ... \otimes H_{int,N}. \tag{4}$$

However, one of the main advantages of the Rydberg array platform is that interactions between atoms can be tuned. As a result, the Hamiltonian is no longer separable and takes form:

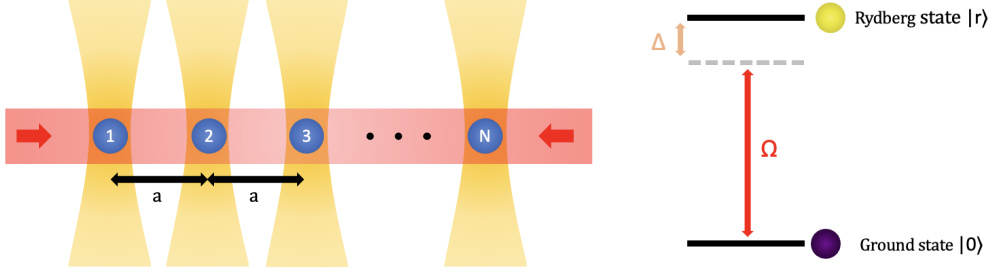$$H = H_{seperable} + H_{ryd\ interaction}. \tag{5}$$

FIG. 1: Atom array and qubit set up Simple schematic showing the experimental set up of trapped atom array and the corresponding two level coupled system for each atom (the qubit). Atoms are held in place by optical tweezers (vertical orange beams) and arranged into 1D array of lattice separation a (range $\approx$ 2-10 μm). Atoms are then driven globally by separate driving lasers (red beam) to couple ^{87}Rb outer electron states $|0\rangle = |5S_{1/2}\rangle$ and $|r\rangle = |70S_{1/2}\rangle$ with effective Rabi frequency Ω and detuning, Δ. This is done via a two photon transition with intermediate level $|e\rangle = |6P_{3/2}\rangle$. For more details see Ref. [7].

2. Interactions between qubits

Characterised by having a single electron in a highly excited state (and thus quantum number n), Rydberg atoms are well approximated by the Bohr model of a hydrogen atom [6]. Using this model, it can be shown that the dipole moment between the outer electron and the rest of the atom scales $\propto n^2$. As a result, Rydberg atoms have significant dipole moment in comparison to their ground state counterparts. The immense dipole leads to strong interactions between Rydberg states. Specifically, two Rydberg atoms in the same Rydberg state will interact via a strong van der Waals interaction of the form:

$$V = \frac{C_6}{R^6},$$

(6)

with $C_6 \propto n^{11}$ the interaction coefficient. Consequently, within our array of qubits, the dipole-dipole interaction is very strong for atoms in the same Rydberg state $|r\rangle$ but negligible for atoms in the same ground state $|0\rangle$. This differentiation is crucial to the dynamics of our simulator as by coupling to the Rydberg state we have an effective way of turning on interactions in our system.

3. The Hamiltonian

With interactions now accounted for, we can construct the many-body Hamiltonian [9]:

$$\frac{H}{\hbar} = \sum_i \frac{\Omega_i}{2}\sigma_i^x - \sum_i \Delta_i n_i + \sum_{k<i} V_{ik} n_i n_k.$$

(7)

The Hamiltonian is in many ways analogous to a canonical one-dimensional quantum Ising Hamiltonian with up and down spins, $|\uparrow\rangle = |0\rangle$ and $|\downarrow\rangle = |r\rangle$ [10]. However, the interactions are long range and act exclusively on Rydberg states, acting as a constraint on nearby excitations. The terms of the Hamiltonian and its significance are as follows:

- $i, 1 < i < N$, corresponds to the position of the atom within the 1D array and is used to label the qubits (see Figure 1).

- The first term is the driving term. It couples the ground and Rydberg states with single qubit operator $\sigma_i^x = |0\rangle_i \langle r|_i + |r\rangle_i \langle 0|_i$ and Rabi frequency Ω_i.

- The second term encodes the single-site detuning through a shift in the energy of the corresponding Rydberg state using projector $n_i = |r\rangle_i \langle r|_i$.

- The last term encodes all the Rydberg-Rydberg state van der Waals interactions within the array. The pairwise interaction is given by $V_{ij} = \frac{C_6}{R^6}$ with $R = a|i - j|$ measuring the separation of the two Rydberg states (a is the lattice separation). This term results in a positive energy shift as the interaction is repulsive.

For our simulations the Rabi frequency is taken to be constant at $\Omega/2\pi = 4.00$ MHz, acting homogeneously on all atoms. Our detuning, on the other hand, will vary through sweeps and be single-site addressed when looking at local quenches. Finally, for our driven Rydberg states $|r\rangle = |70S_{1/2}\rangle$ the interaction coefficient is taken as $C_6 = 863$ x 2π GHz μm^6 [7, 11].

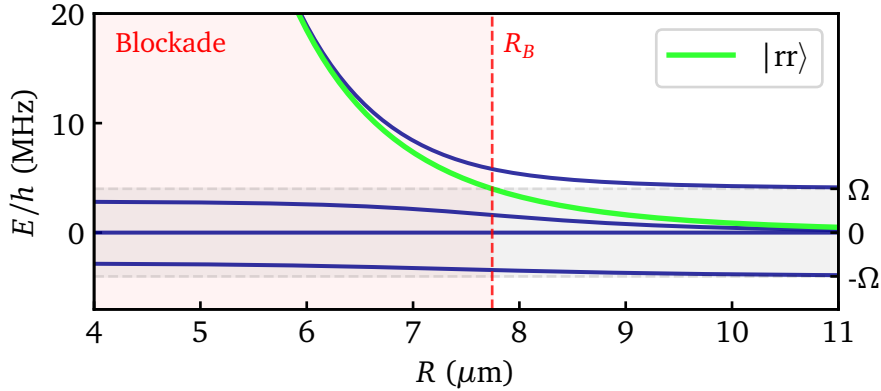### 4. Constraints: Rydberg blockade

FIG. 2: Two atom eigenenergies and Rydberg blockade Eigenenergies of the two atom Hamiltonian are shown in dark blue and plotted against spatial separation of two atoms R. The green line indicates the expectation energy of the doubly excited Rydberg state $|rr\rangle = |r\rangle_1 \otimes |r\rangle_2$ given by $|\langle rr|H|rr\rangle|^2$. This value is equivalent to the energy shift given by the van der Waals interaction: $|\langle rr|H|rr\rangle|^2 = V_{1,2} = C_6/R^6$. We defined separation $R = R_B$, such that $C_6/R_B^6 = \Omega$, the *blockade radius*. The *blockade radius* is shown in the figure by the red dashed line. For separations $R \leq R_B$ the transition to the doubly excited Rydberg state becomes increasingly unlikely as the energy difference is greater than Ω. As a result, the red region of the figure is know as the blockaded region (the $|rr\rangle$ transition is 'block' off). Moreover, the lower eigenenergies are also shifted in this region as the $|rr\rangle$ state decouples from the system.

The van der Waals interaction results in an energy shift of eigenstates of the Hamiltonian with nearby Rydberg excitations. To demonstrate, eigenstates of the two atom Hamiltonian

are plotted against varying atomic separations R in Figure 2. Included in the figure, is the expectation energy of the $|rr\rangle$ state, which due to the Rydberg van der Waals interaction Eq. (6), is $\propto 1/R^6$. This rapid increase in energy of the $|rr\rangle$ state with decreasing atomic separations results in a phenomenon known as Rydberg blockade, whereby for close enough separations, $R < R_B$, the driving laser cannot excite both atoms to the doubly excited Rydberg state $|rr\rangle$.

As a result of the blockade effect, within $R < R_B$ the laser couples states $|00\rangle$ and $|\Psi^+\rangle = \frac{1}{\sqrt{2}}(|0r\rangle + |r0\rangle)$ with a Rydberg excitation is shared amongst the two qubits. The other $|\Psi^-\rangle = \frac{1}{\sqrt{2}}(|0r\rangle - |r0\rangle)$ Bell state is uncoupled by parity conservation. Consequently, the blockade mechanism will enable us to put constrains on the system and generate entanglement. Before then, we briefly discuss how we can evolve the Hamiltonian in time to study the dynamics of the effect.

B. Evolving the system

1. Trotter-Suzuki decomposition

To study time dependent phenomena, the state vector can be evolved using Trotter-Suzuki decomposition [12]:

$$|\psi(t)\rangle = \prod_{i=1}^{n} e^{-iH[\Omega(t_i),\Delta(t_i)]dt_i} |\psi(0)\rangle, \tag{8}$$

which solves Schrödinger's equation iteratively with time step $dt_i = t_i - t_{i-1}$ and inital state $|\psi(0)\rangle$.

In this work, the Hamiltonian undergoes evolution by sweeping through detuning values, Δ. Starting from an initial ground state $|\psi(0)\rangle$, the rate of these detuning sweeps dictates whether the evolution proceeds adiabatically. This is a consequence of the adiabatic theorem: a quantum system stays in its instantaneous eigenstate if parameters of the Hamiltonian are evolved slow enough and there is an energy gap between eigenstate and the rest of the spectrum [1].

In later sections, quenching the system will involve sweeping through detuning values very quickly such that the adiabatic theorem breaks down and multiple diabatic transitions to higher energy eigenstates occur.
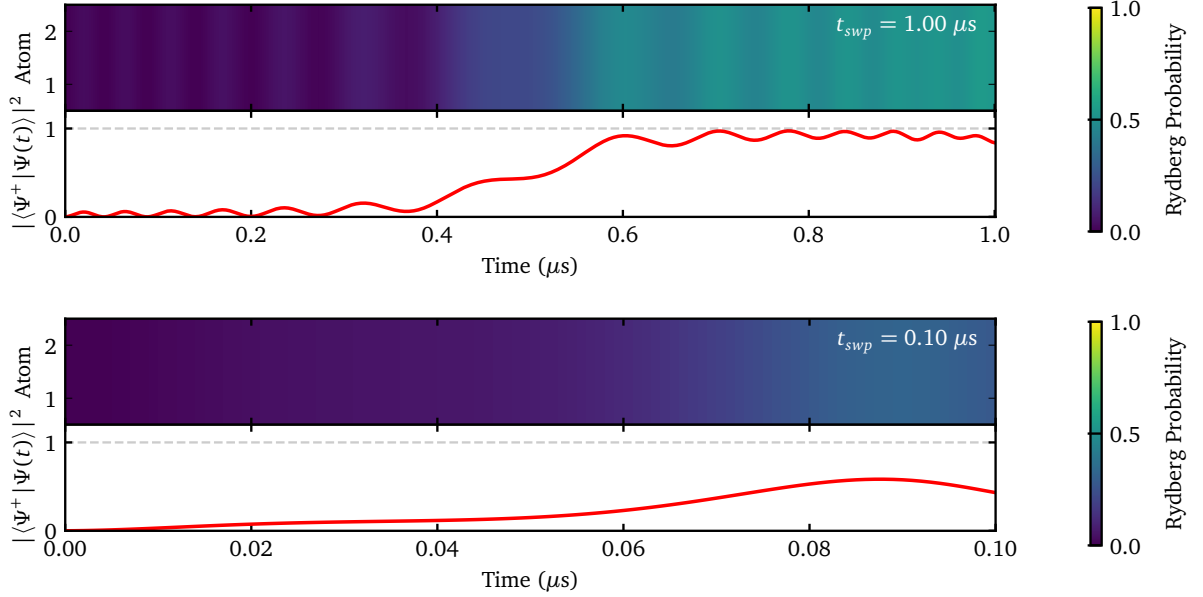
2. Two atom sweeps

To demonstrate the evolution of the system by sweeping detuning values and to showcase the Rydberg blockade mechanism in effect, we prepare the $|\Psi^+\rangle = \frac{1}{\sqrt{2}}(|0r\rangle + |r0\rangle)$ Bell state using two different sweep rates on a two atom array with $a < R_b$ and initial state $|\Psi(0)\rangle = |00\rangle$.

By linearly increasing the detuning Δ from negative to positive, Rydberg excitations are progressively favoured (See Figure 3). However, since both atoms are within each others blockade radius, the transition to the $|rr\rangle$ state is blocked off. Consequently, at high detuning levels, the $|\Psi^+\rangle$ Bell state is favoured, characterised by a single shared excitation.

(a) Linear sweep regime
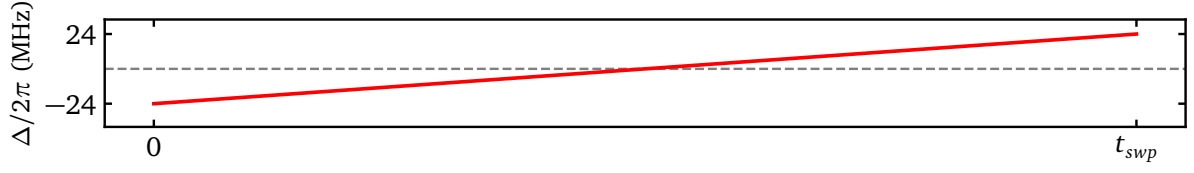
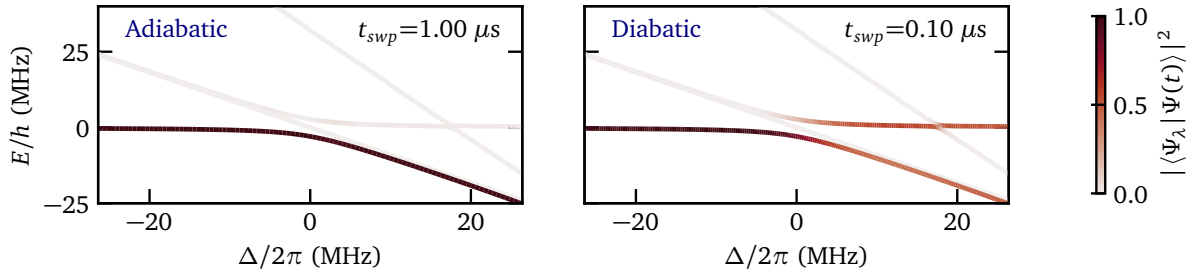**(b) Bell state preparation fidelities**

(c) Eigenenergy spectrum

FIG. 3: Two atom adiabatic vs diabatic detuning sweeps Linear detuning sweeps from $\Delta/2\pi$ = -24.0 MHz to $\Delta/2\pi$ = 24.0 MHz preformed globally on two atom system with respective sweep times t_{swp} 1.00 μs (adiabatic) and t_{swp} 0.01 μs (diabatic) . Detuning sweeps shown in **(a)**. Colormaps of single site Rydberg excitation probability, $\langle n_i \rangle$, along with corresponding two atom Bell state fidelity $|\langle \Psi^+ | \Psi(t) \rangle|^2$ (red line) shown in **(b)**. In both sweep cases, single site Rydberg excitation probability is bounded above by 0.5 due to the Rydberg Blockade constraint. Finally in **(c)**, eigenenergy spectrum of the 4 eigenstates of the two atom system are shown. Colormap on spectrum indicates the dynamics of the individual eigenstate fidelities $|\langle \Psi_\lambda | \Psi(t) \rangle|^2$ as the system is swept through detuning values. Throughout the evolution, Rabi frequency is kept constant at $\Omega/2\pi$ = 4.00 MHz and a time step of dt = 0.001 μs.

In Figure 3, this process is done for two different sweep rates to demonstrate the difference between adiabatic and diabatic sweeps. For the adiabatic sweep (t_{swp} = 1.00 μs), the system remains in the ground state with >99.9% fidelity for the entire evolution, resulting in final average Bell state fidelity 98.1%. The difference arises from the fact that the final ground state of the system in not a perfect Bell state due to the tiny couplings between states $|00\rangle$ and $|\Psi_+\rangle$ still present in the system. This can been seen in the figure by the small oscillations of the Bell state fidelity.

In the diabatic case (t_{swp} = 0.01 μs), the system evolves quickly through its eigenenergy spectrum (See Figure 3c). At the critical point $\Delta/2\pi$ = 0.00 MHz, a portion of the state transitions from the ground state $|\psi_0\rangle$ to the higher energy eigenstate $|\psi_3\rangle$. This is a consequence of the breakdown of the adiabatic theorem which results in a diabatic transition. The same process occurs at crossing between eigenstates at $\Delta/2\pi \approx 19$ MHz, leaving the Bell state to be prepared with $\approx 50\%$ as about half the state vector is not in the ground state.

3. Rydberg crystals

Finally, building on the two atom example, we demonstrate how adiabatically sweeping detuning from negative to positive can also be used to generate spatially ordered Rydberg excitation states on our array for the purposes of quenching them later.

At high positive detuning, $\Delta >> 0$, the ground state will maximise number of the Rydberg excitations subject to the Rydberg blockade constraint. Using optical tweezers, the separation of atoms can be adjusted, enabling the modification of the number of atoms within each other's blockade radius, R_B. This results in the emergence of order states Z_n, characterised by transnational symmetry of n atomic sites. These states are know as Rydberg crystals [7] and in Figure 4 we give a a qualitative presentation.

In the case of even N arrays, these states are degenerate due to symmetry. For example, at nearest neighbour (NN) interaction, states $Z_2 = |r0r0r...\rangle$ or $|0r0r0...\rangle$ emerge with equal probability. Whereas for odd N arrays, since high detuning maximises the number of Rydberg

Z_2 Crystal: Nearest neighbour (NN) blockade, $V_{i,i+1} > \Delta >> V_{i,i+2}$, $|\Psi\rangle = |r0r0r...\rangle$.

Z_3 Crystal: Next-to-nearest neighbour blockade, $V_{i,i+2} > \Delta >> V_{i,i+3}$, $|\Psi\rangle = |r00r0...\rangle$.
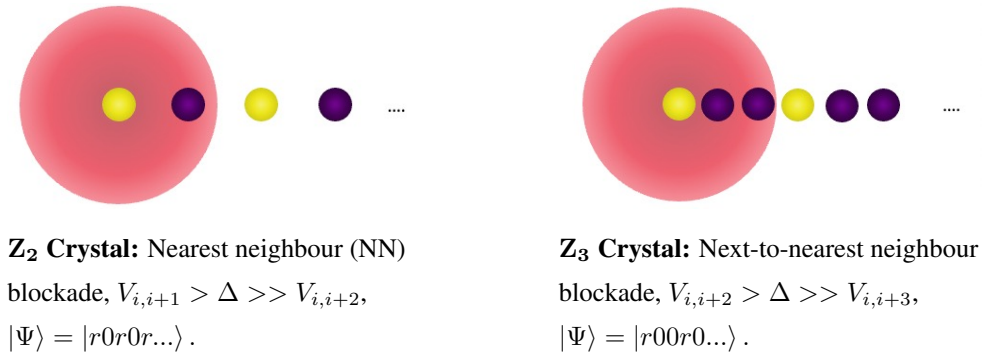
FIG. 4: Ordered Rydberg crystalline states Schematic of order states which form at positive detuning, $\Delta > 0$ subjected Rydberg blocked constraints. Bright yellow dot represents atom in Rydberg state $|r\rangle$ and dark purple dot represents atom in ground zero state $|0\rangle$. Red outline indicates blockade radius R_b in which all atoms are constrained to one Rydberg excitation.

excitations, the ground state is non-degenerate. In the 3 atom case the two Z_2 symmetry states are $|r0r\rangle$ and $|0r0\rangle$, but the $|r0r\rangle$ ends up as the ground state due to the additional excitation.

Throughout this work we will focus on odd N arrays to eliminate the explicit degeneracy of the high detuning ground state. Moreover, when we refer to the Z_n state, we will refer to the high detuning ground state with the maximum number of Rydberg excitations (this will be the state with edge Rydberg excitations). For example, Z_2 will refer to the state $|r0r\rangle$ in the three atom case, not the $|0r0\rangle$ state.

In the same way that the two atom Bell state was prepared by adiabatically sweeping detuning from negative to positive, we can use the same protocol to generate the Rydberg crystal states. Starting from the easily initialised, large negative detuning, ground state $|000...\rangle$ which we will refer to as the $Zeros$ state, we can sweep to large positive detunings such that the crystal states emerge with high fidelity subject to the Rydberg constraint (see Figure 5). The generation of these crystal states is an example of a quantum phase transition - the transitioning between two states of matter solely by quantum fluctuations (at zero temperature) [13].
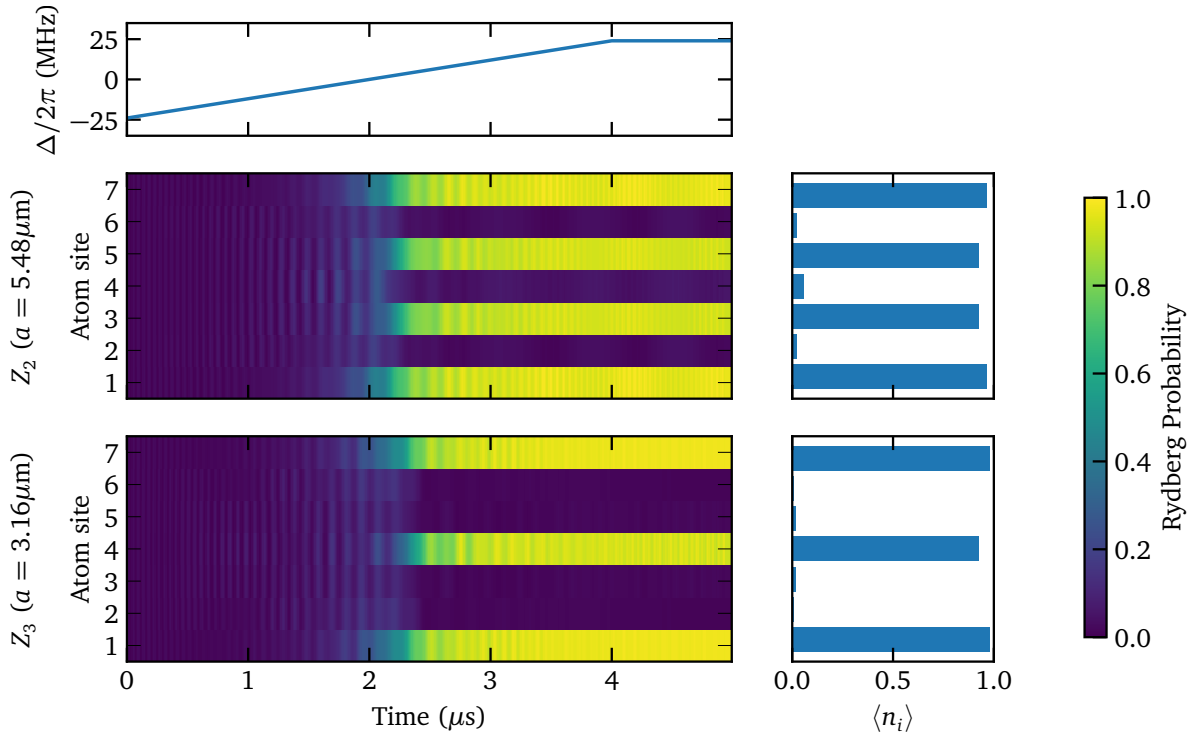

FIG. 5: Generating Rydberg Crystals 7 atom Rydberg crystals are prepared by adiabatically sweeping from large negative detuning $\Delta/2\pi$ = -24.00 MHz to large positive detuning $\Delta/2\pi$ = 24.00 MHz linearly and at constant Rabi frequency $\Omega/2\pi$ = 4.00 MHz. Two lattice separations a = 5.48 μm and a = 3.16 μm are considered such that Z_2 and Z_3 crystals are generated respectively. Separation a = 5.48 μm, $V_{i,i+1} > \Delta >> \Omega >> V_{i,i+2}$ results in nearest neighbour blockade (Z_2 ground state). Whereas, separation a = 3.16 μm with $V_{i,i+2} > \Delta >> \Omega >> V_{i,i+3}$ results in next-to-nearest neighbour blockade (Z_3 ground state).

When we begin quenching the array we will focus on the Z_2 crystalline state, due to its association with quantum many-body scarring behaviour and its interesting quantum transport dynamics. To assist the study of the Z_2 quench, we investigate the detuning values in which the Z_2 appears with the highest ground state fidelity (See Figure 6).

An important result we highlight from the figure, is that even at high enough detuning where anti-blockade starts to take effect ($|rr\rangle$ transition is allowed, $\Delta \geq V_{NN}$), the Z_2 order state remains a ground state of the system with high fidelity. It is not until very high detunings of $\Delta \approx 2V_{NN}$ that this breaks downs. This is because adding an additional Rydberg excitation to the Z_2 state will result in two strong NN interactions, increasing the energy of state by $+2V_{NN}$. The distinction is made clear as in the local quench section, we will compare quenches from within the blockade region ($|rr\rangle$ state is not allowed) vs quenches within the anti-blockade region ($|rr\rangle$ state is allowed).
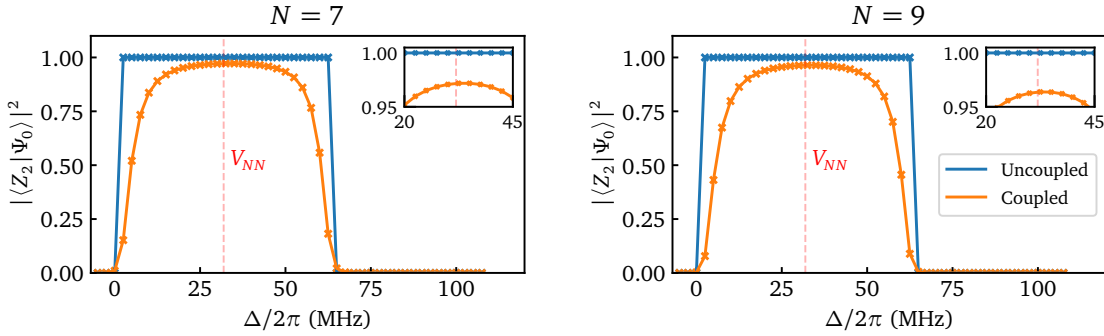

FIG. 6: **Ground state Z_2 fidelity vs positive detuning** To understand where Z_2 ordered state emerges, we calculate the ground state Z_2 fidelity, $|\langle Z_2|\Psi_0\rangle|^2$, across Hamiltonians with detunings between $\Delta/2\pi$ = -5.00 MHz and $\Delta/2\pi$ = 110.00 MHz, increasing in increments of $\Delta/2\pi$ = 2.5 MHz. We compare the results of the coupled (Ω = 4.00 MHz, orange) and uncoupled (Ω = 0.00 MHz, blue) Hamiltonians to demonstrate the slight damping of state fidelities the coupling has. Using the results of this figure, we can determine detuning ranges to keep the system in, if we want to attain the Z_2 state with maximum fidelity. In both $N = 7$ and $N = 9$ arrays we note that in the range 23.0 MHz $< \Delta/2\pi <$ 40.0 MHz the Z_2 state is the ground state with upwards of 95% fidelity. The maximum fidelity of the Z_2 for the coupled Hamiltonian is attained near the anti-blockade detuning $\Delta/2\pi = V_{NN}/2\pi = 31.9$ MHz indicated by red dashed lines on the figures.

3.   QUANTUM ENTANGLEMENT MEASURES

In the previous section, by projecting onto the z-axis of each qubit, we measured the probability of each atom being in the Rydberg state $|r\rangle$, enabling us to demonstrate the formation of the Z_n spatial ordered states at high detuning. However, when we begin quenching the array, our state vector will be propelled into a superposition of different states, leading to a build up of entangled states. Consequently, the reductive nature of the single site Rydberg fidelity measurements fails to fully describe the dynamics of the strongly correlated post-quench system. To overcome this, we briefly introduce two entanglement measures within quantum information theory: the *von Neumann entropy* and the *concurrence*. These measures will be used to gain a

more comprehensive understanding of the out-of-equilibrium dynamics elicited by the quench. Before then, we quickly review what is meant by entanglement within the context of our system.

A. Entangled states

It is a postulate of quantum mechanics that all the information about a closed system is encoded into the state vector $|\psi\rangle$ [1]. In the case of the N qubit array, the state vector lives in an 2^N dimensional Hilbert space. Whilst building up the Hamiltonian of the system, we stressed that due to interactions between qubits, namely the Rydberg-Rydberg van der Waals interaction, the Hamiltonian could not necessarily be partitioned locally:

$$H \neq H_1 \otimes H_2 \otimes ... \otimes H_N. \tag{9}$$

Similarly, if we consider our state vector for the whole system $|\psi\rangle$, the same applies:

$$|\psi\rangle \neq |\psi\rangle_1 \otimes |\psi\rangle_2 \otimes ... \otimes |\psi\rangle_N. \tag{10}$$

This essentially means that the information about the system cannot always be split into its individual qubit parts $|\psi\rangle_i$; even though the qubits themselves are separate in physical space. This strange phenomenon is know as quantum entanglement and it leads to the formation of non-local correlations throughout the array. A quintessential example of the this is the two qubit Bell state we prepared in Figure 3:

$$|\Psi_+\rangle = \frac{1}{\sqrt{2}}(|0r\rangle + |r0\rangle) = \frac{1}{\sqrt{2}}(|0\rangle \otimes |r\rangle + |r\rangle \otimes |0\rangle) \neq |\psi\rangle_1 \otimes |\psi\rangle_2. \tag{11}$$

B. Entanglement entropy

Quantifying entanglement on the array, will involve using a more general description of the quantum state of the system and its subsystems coming from quantum statistical mechanics: the density matrix ρ (see Appendix B for supplementary details). Unlike the state vector, the density matrix description of a quantum state is statistical and considers an ensemble of different

FIG. 7: Partitioning 7 atom array To demonstrate how the state of system can be reduced, we give an illustrative example of dividing the 7 Atom array, described by state vector $|\psi\rangle$, into two parts. In the schematic above, the first four qubits form subsystem A and the last 3 qubits subsystem B. The respective subsystems can be described by reduced density matrices: $\rho_A = tr_B(\rho)$ and $\rho_B = tr_A(\rho)$ with $\rho = |\psi\rangle \langle\psi|$. The bipartite entanglement between A and B can be quantified using von Neumann entropy: $S_{EE}(\rho_A) = -tr[\rho_A ln(\rho_A)] = S_{EE}(\rho_B)$ giving a non zero value if $|\psi\rangle \neq |\psi\rangle_A \otimes |\psi\rangle_B$.

potential state vectors. In doing so the density matrix can describe both pure and mixed quantum states.

A useful feature of density matrices is that we can gain information about subregions of an entangled system. Imagine we partition our array into two sub regions A and B consisting of N_A and N_B qubits. If these two subregions where entangled in anyway, we would not be able to split the system up into two state vectors, $|\psi\rangle \neq |\psi\rangle_A \otimes |\psi\rangle_B$. However, using density matrices we can formulate a statistical description of A and B. This is done using reduced density matrices which are defined as follows:

$$\rho_A = tr_B(\rho), \quad \rho_B = tr_A(\rho), \tag{12}$$

where tr_i denotes the partial trace, $\rho = |\psi\rangle\langle\psi|$ the density matrix of the entire pure system and ρ_X the reduced density matrices ($X = A$, B). It's important to note that the reduced density matrices ρ_X does not give a full description of the state of the respective subsystems. They tell us as much as we can learn about subsystem X by just looking at X and ignoring the correlations with the other subsystem X'. For a demonstrative example of how the Rydberg array can be partitioned, see Figure 7.

With the reduced density matrix in mind, we introduce our first and most recognised measure of entanglement: the von Neumann entropy [14] . The von Neumann entropy is a measure of the bipartite entanglement between two parts of a closed, pure quantum many-body system and is defined as follows:

$$S_{EE}(\rho_X) = -tr[\rho_X ln(\rho_X)], \tag{13}$$

where ρ_X is the reduced density matrix of the respective subsystems ($X = A$, B) of the pure state, $\rho = |\psi\rangle\langle\psi|$.

Deriving it's definition from information theory, namely Shannon entropy, the von Neumann entropy measures the uncertainty of the information provided by the reduced density matrix, ρ_X. In doing so, it quantifies the amount of information about X that must be associated with X' and hence the entanglement between the two subsystems.

Before we move on to the next entanglement measure, we note some key features:

- $S_{EE}(\rho_A) = S_{EE}(\rho_B)$.

- $S_{EE}(\rho_A) = 0 \iff \rho_A$ is pure $\iff$ subsystem A and B are separable (unentangled).

- $0 \leq S_{EE}(\rho_A) \leq log(\widetilde{D})$ where $\widetilde{D} = min\{2^{N_A}, 2^{N_B}\}$ is the smallest reduced density matrix dimension.

- $S_{EE}(\rho_A) = log(\widetilde{D}) \iff$ A and B are maximally entangled.

From now on, when we refer to entanglement entropy (given the shorthand of EE), we will be referring to specifically the von Neumann entropy.

Lastly, for the purposes of our work, the exact value of the EE will not be important. Instead, the relative scaling and growth of the EE amongst atom sites is studied. By quantifying how entangled information is amongst subsystems of the array, EE gives us with a powerful way of determining how information spreads the and how the complexity of the system grows.

C. Concurrence

The von Neumann entropy is useful for quantifying entanglement between bipartitions of a pure state. However, in our later work, we will see that bipartiting the entire pure state of the system will not allow us to quantify how localised entanglement is on our system. As a result, we look for ways to quantify entanglement on subregions of our system and hence on mixed states. Methods of quantifying the entanglement within mixed states are much more complicated as the exact state of the system is statistically uncertain. However, there is an entanglement measure which does a good job at describing the pairwise entanglement between two qubits given by a density matrix ρ (both pure and mixed). This entanglement measure is the concurrence and is defined as follows [15]:

$$C(\rho) = max\{0, \lambda_1 - \lambda_2 - \lambda_3 - \lambda_4\}, \tag{14}$$

where λ_i are the eigenvalues of the matrix $R = \sqrt{\sqrt{\rho}\widetilde{\rho}\sqrt{\rho}}$ and $\widetilde{\rho}$ is the so called spin flipped density matrix $\widetilde{\rho} = (\sigma_y \otimes \sigma_y)\rho^*(\sigma_y \otimes \sigma_y)$. The concurrence ranges between 0 for a separable state and 1 for the maximally entangled two qubit Bell states. For more details, see Ref. [15].

It is important to stress that this is a measurement of the pairwise entanglement between two qubits. If we have an array of 3 qubits in a maximally entangled GHZ state $|GHZ\rangle = |000\rangle + |rrr\rangle$, the concurrence of any pair of qubits $C(i, j)$ will be zero even though all the qubits are clearly entangled. As a result, the concurrence is very much a measure of the locality of entanglement between two qubits. We will see the importance of this measure when performing local quenches on our array.

4. GLOBAL QUENCH

In Ref. [7], it was found that rapidly dropping the global detuning of the driving laser to the critical point, $\Delta/2\pi = 0.00$ MHz, resulted in surprising oscillatory revivals of the Z_2 initial ground state. The behaviour was called quantum many-body scaring and has challenged concrete ideas about quantum thermalisation [8].

To highlight the significance of the result and, in turn, to demonstrate the potential of the Rydberg atom array in investigating out-of-equilibrium phenomena, we study the underlying dynamics of this behaviour.

A. Single-site Rydberg probabilities

The unique behaviour of the Z_2 quench is demonstrated in Figure 8 on a 7 atom array. Unlike the quench of the 7 atom $Zeros$ state, ordered oscillation of the initial Z_2 state are observed after quench. They persist with peak fidelities >35% for timescales up to ≈ 2 μs; much longer than any natural time scale set by the system, in particular time scale set by Rabi frequency $1/\Omega = 0.25$ μs. Considering that the Rydberg Hamiltonian posses no inherent symmetries [16] and the behaviour following the aggressive quench is expected to be disordered, this ordered behaviour is very surprising. It is even more surprising that this behaviour has been demonstrated and even

controlled on 2D arrays of up to 200 interacting Rydberg qubits (revivals in a 2^{200} dimensional Hilbert space) [17].

(a) Z_2 state global quench
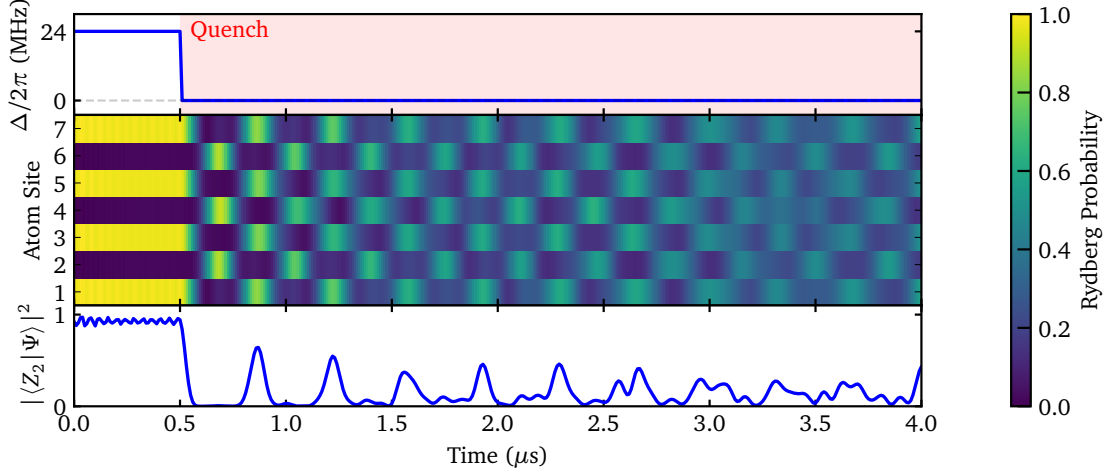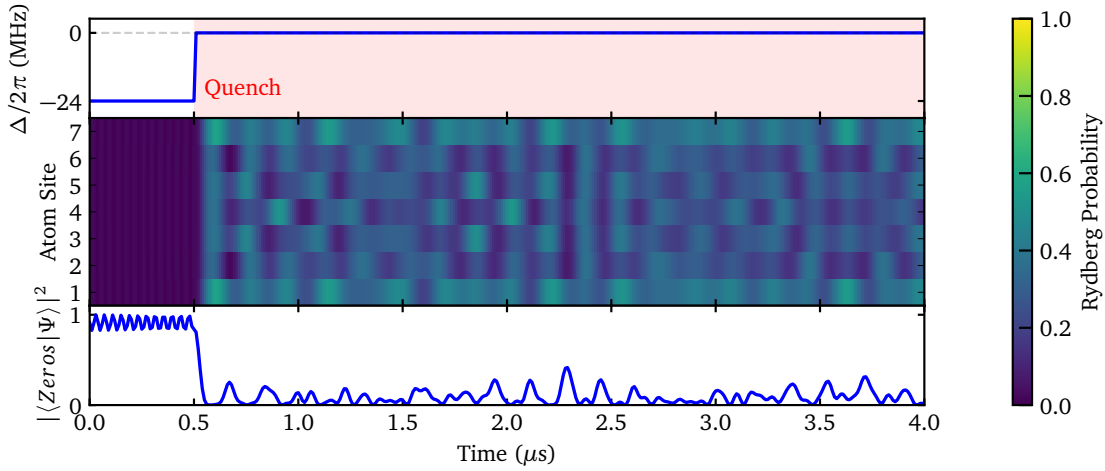

(b) Zeros state global quench

FIG. 8: Global quench and quantum many-body scars All atoms in array are quenched uniformly by rapidly changing initial global detuning to critical point $\Delta/2\pi = 0.00$ MHz over single time step $dt = 0.01$ μs with Rabi frequency kept constant at $\Omega/2\pi = 4.00$ MHz. Lattice separation is set to $a = 5.48$ μm such that nearest neighbour blockade is present with $V_{NN}/2\pi = 31.9$ MHz. Time of quench is $t = 0.50$ μs. In **(a)**, quench of $Z_2 = |r0r0r0r\rangle$ ordered state is performed from initial ground state configuration at positive detuning $\Delta/2\pi = 24.0$ MHz. Regular oscillatory revivals of the Z_2 state are observed after quench (*quantum many body scars* effect). Result is compared to quench of $Zeros = |0000000\rangle$ state from initial ground state configuration at negative detuning $\Delta/2\pi = -24.0$ MHz in **(b)**, where no such oscillations are observed. The comparison highlights the unique behaviour of the Z_2 quench.

In the following subsections, we will look at the spreading of the initial state vector across the eigenenergy spectrum and how its entanglement entropy scales after the quench. We stress that this will not do full justice to a lot of the deeper concepts surrounding quantum many-body scars. Rather, we showcase underlying characteristics which are/could be associated with the scar behaviour. A lot of the work focusing on quantum many body scars has looked at the PXP Hamiltonian model of the Rydberg atom array (see Ref. [8, 16] for details). We hope instead that our work might shed some light on interesting underlying dynamics of the solution space of the 1D Rydberg Ising-type Hamiltonian Eq. (7).

B. Eigenenergy spectrum

To further understand the quantum many-body scaring effect within the context of our system, we study the eigenenergy spectrum of the states following the Z_2 and $Zeros$ quenches (see Figure 9). Like we saw with the diabatic sweep in Figure 3, the quench results in the state of the system spreading across higher energy eigenstates of the 2^7 dimensional Hilbert space. Significantly, we observe that this spreading is restricted to a smaller 34 dimensional eigenenergy manifold, highlighted in orange on the figure. It is reasonable to assume this manifold is associated with the nearest neighbour blockade constraint at $\Delta/2\pi = 0.00$ MHz.

In addition, for the specific case of the Z_2 quench, the spreading across eigenstates is unusually ordered (see inset Figure 9a). In particular, when ignoring eigenstates with fidelities less than 1% , we find that the resulting state of the system is made up of only 6 eigenenergies. Even more significantly, these eigenenergies are uniformly separated with average energy separation $E/h = 2.77$ MHz and standard deviation 0.09 MHz.
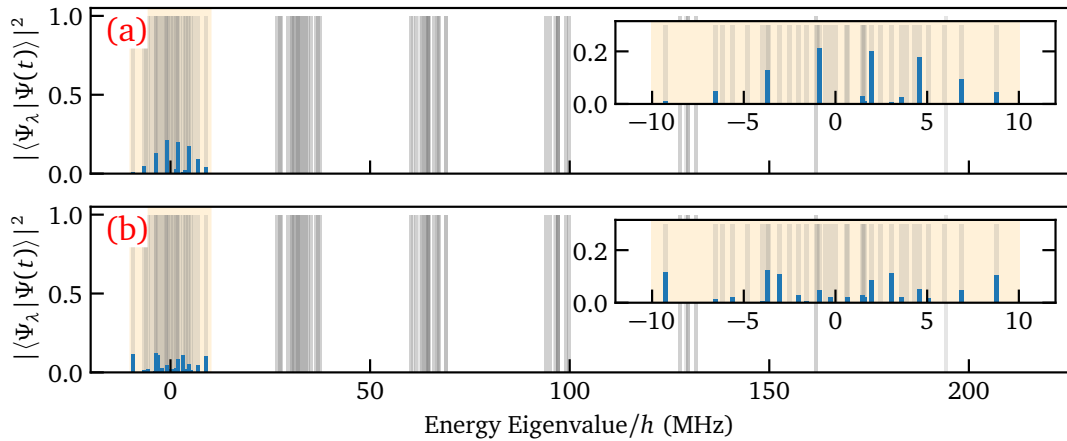

FIG. 9: **Post-quench eigenenergy spectrum** Eigenenergy spectrum is demonstrated following quenches performed in Figure 8 for Z_2 **(a)** and $Zeros$ **(b)** initial states. Spectrum is made up of the 2^7 eigenenergies of zero detuning Hamiltonian (grey lines). Blue bars show the individual energy eigenstate fidelities of the post-quench state, $|\langle \Psi_\lambda | \Psi(t) \rangle|^2$. Eigenstate fidelities are constant in time as are stationary states of the time independent post-quench Hamiltonian. The orange region indicates constrained region of eigenenergy spreading with fidelities $> 0.001\%$. Lastly, ordered spreading of Z_2 post-quench state is visible in the inset of **(a)**.

The exact origins of this ordered behavior are unclear. However, when considering that the evolution of the quenched system can be described as an evolution of the eigenstates $|\psi_\lambda\rangle$ of the zero detuning Hamiltonian:

$$|\Psi(t)\rangle = \sum_\lambda^N c_\lambda e^{\frac{-iE_\lambda t}{\hbar}} |\psi_\lambda\rangle, \tag{15}$$

with eigenenergies E_λ and eigenstate fidelities $|c_\lambda|^2 = |\langle\psi_\lambda|\Psi(t)\rangle|^2$, it is reasonable to assume this order arrangement of eigenenergies carries some connection to the ordered revivals of the Z_2 state following its quench. This is supported by the contrasting chaotic spreading of the $Zeros$ state after the quench (see inset Figure 9b).

C. Entanglement entropy growth and scaling

So far the results have been projective, reducing the system down and ignoring the correlations that emerge due to interaction. To overcome this, we measure the growth and the scaling of entanglement entropy (EE) following the global quench of the respective Z_2 and $Zeros$ state cases (See Figure 10).

In both quench cases, the half chain EE grows linearly before saturating around a value $< ln(2^3)$ (See Figure 10a) . This growth is associated with the formation of correlations along the array as the system is propelled into a superposition of eigenstates that are entangled by the Rydberg blockade mechanism. Moreover, we can associate the initial linear growth and delayed saturation with the time it takes for correlations to travel across the system [18]. Therefore, it is interesting that the saturation time is approximately 3 times greater in the case of the Z_2 quench.

Furthermore, we study how the bipartite EE, $S_{EE}(\rho_A)$, scales as we increase the size of subsystem A across the chain (See Figure 10b). Typically, on a strongly correlated system such as ours, we would expect EE to scale with the corresponding sizes of the subsystems (maximised at half chain splitting $N_A = 4$ (3) and $N_B = 3$ (4)). This scaling is referred to as a volume law and is apparent at $t = 0.40\,\mu$s for the $Zeros$ state and $t = 0.80\,\mu$s for both initial states. Interestingly, at $t = 0.40\,\mu$s, the EE following the Z_2 state quench doesn't follow a volume but instead an area law, $S_{EE}(\rho_A) \propto const$ [19].

Combining these observations together, we can infer a couple features about the quantum many-body scaring behaviour. Firstly, the significantly slower growth of the half chain EE following the Z_2 state quench could render revivals of the initial unentangled state more likely as the system is initially made up of fewer entangled states. In fact, the decay of the Z_2 fidelity peaks over the timescale of $\approx 1.5\,\mu$s (see Figure 8) is reflected by the linear growth of the EE on this timescale. Secondly, we note that the prolonged area law scaling of the Z_2 initial state is reminiscent of behaviour found in quantum states with many body localisations (MBL), where, due to localisation, information does not spread across the whole system [20]. Hence the system retains close knowledge of it's initial state. Now, the state following the Z_2 quench is not a MBL (it exhibits a volume law at later times) but it's prolonged area law scaling would impart a constraint on the available states the system could be in and hence potentially result in the Z_2 state reappearing with high fidelity.
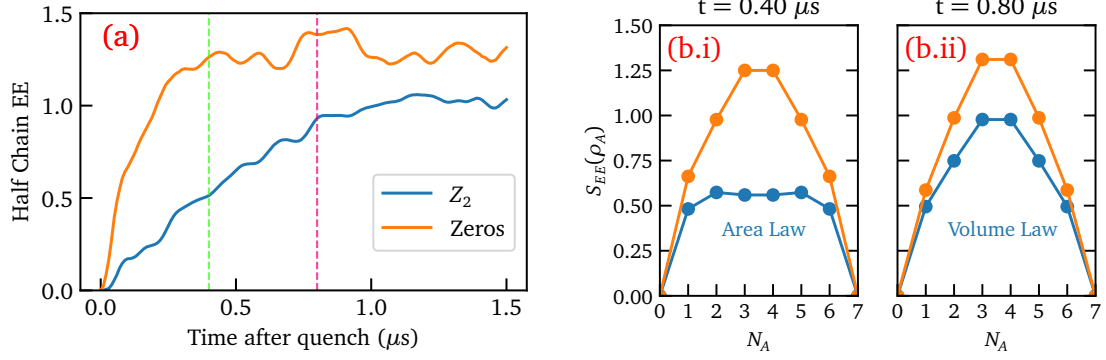
FIG. 10: Entanglement entropy growth and scaling Growth of half chain entanglement entropy following global quenches of initial states Z_2 (blue line) and $Zeros$ (orange line) in Figure 8 are shown in **(a)**. Half chain entanglement entropy is calculated by considering a bipartite splitting of the array between the first four qubits and last three qubits. Then the von Neumann entropy (EE) is calculated between the two subsystems: $S_{EE}(\rho_{1-4}) = S_{EE}(\rho_{5-7})$. Scaling of the entanglement along the array is shown for the two quench cases at timestamps $t = 0.40$ μs **(b.i)** and $t = 0.80$ μs **(b.ii)** corresponding respectively to the timestamps of the green and pink lines in **(a)**. Scaling is quantified by increasing the size of subsystem A (N_A qubits) along the array, starting from 0 and finishing at atom 7. For each additional qubit, the EE between A and the rest of the array is calculated: $S_{EE}(\rho_A)$. At $t = 0.40$ μs **(b.i)** area law scaling, $S_{EE}(\rho_A) \propto const$, is clear for the Z_2 case and not the $Zeros$. At $t = 0.80$ μs **(b.ii)** both cases saturate to a volume law, characterised by peak at half chain splitting, $N_A = 3, 4$.

D. Outlook

Overall, by globally quenching the system, we introduce quantum many-body scars, a novel out-of-equilibrium dynamic for closed quantum systems. By studying the eigenenergy spectrum following the quench, we find that this behaviour could be related to the uniform spreading of the post quench state across a constrained eigenenergy manifold. Building on this idea, we found further constraining dynamics associated with the slow growth and prolonged area law scaling of entanglement entropy. Now, it is unclear the extent to which these constraints are connected to the quantum many-body scaring behaviour. However, we stress that it displays the compelling, rich dynamics which can be explored by taking the Rydberg atom array out-of-equilibrium,

Additionally, we recognise the exciting field of research prompted by quantum many-body scaring. Primarily, quantum many-body scars give a counter example to the eigenstate thermalisation hypothesis which describes how large non-integrable quantum many-body system can thermalise to a state that closely reflects a statistical equilibrium ensemble [16]. Understanding the mechanisms behind this behaviour could uncover deeper connections between quantum mechanics and statistical mechanics. On the other hand, quantum many body scar states could have a place in developing robust quantum systems - the delayed thermalisation of scar states could mitigate errors arising from external noise. In fact, work already has been done controlling and extending the lifetime of the scaring behavior [17].

5. LOCAL QUENCH

To further demonstrate the potential of the Rydberg atom array as a gateway to studying out-of-equilibrium quantum dynamics, quenches are performed on subsets of the array. Through this inhomogeneous quench, we observe compelling quantum transport phenomena associated with the way information and entanglement propagate throughout the array.

To aid this study, we increase array size to N = 9 atoms, giving a larger platform to probe the propagation dynamics. Moreover, after observing the unique scar behaviour following the Z_2 global quench, we focus our attention on local quenches of this initial state, with strong nearest neighbour (NN) interactions.

A. Quenching the edge atom

To begin the investigation, we quench solely the edge atom of the array. This enables us to use the rest of the unperturbed 8 atoms to investigate how information about the quench spreads throughout the system. To start with, we look at the single-site Rydberg state fidelities.

1. Single-site Rydberg probabilities

In Figure 11a, the detuning at atom site 1 is brought down rapidly, quenching the system. Following the quench, a light-cone like sequential change in Rydberg fidelities is observed throughout the array from the quench site. The behaviour forms a wavefront between the initial ordered Z_2 state and a mixture of disorder states. Surprisingly, the propagation wavefront appears to reflect off the other edge atom and cancel itself out as it propagates back in the opposite direction, restoring part of the Z_2 state.

Motivated by the dynamics of this behaviour, we examine the dependency of this phenomenon on the initial detuning, $\Delta_{t=0}$, and correspondingly the detuning across the remaining unquenched array, Δ_{2-9}. We focus on initial detuning values, $\Delta_{t=0}$, such that the Z_2 state is a prequench ground state with fidelities $> 96\%$. Additionally, we consider detuning beyond the nearest neighbour blockade condition, $\Delta_{t=0} = \Delta_{2-9} > V_{NN}$, to study how the blockade mechanism changes the dynamics. In Figure 11b, we highlight the different behaviour that emerges with 4 additional simulations.

For all the quenches, the individual qubit's Rydberg fidelities change within an effective light cone from quench site. However, the behaviour of the initial light cone wavefront varies significantly from detuning case to case. Specifically, we highlight the case where detuning is set to the NN interaction, $\Delta_{t=0} = V_{NN}$ (anti-blockade boundary). Unique to the other quench cases, we observe that the fidelity wavefront is compact and wave packet-like with transitions between the two Z_2 order states oscillating in time. The narrowing of this behaviour around the anti-blockade condition is suggestive of a unique resonance associated with locally perturbing the array at this detuning.

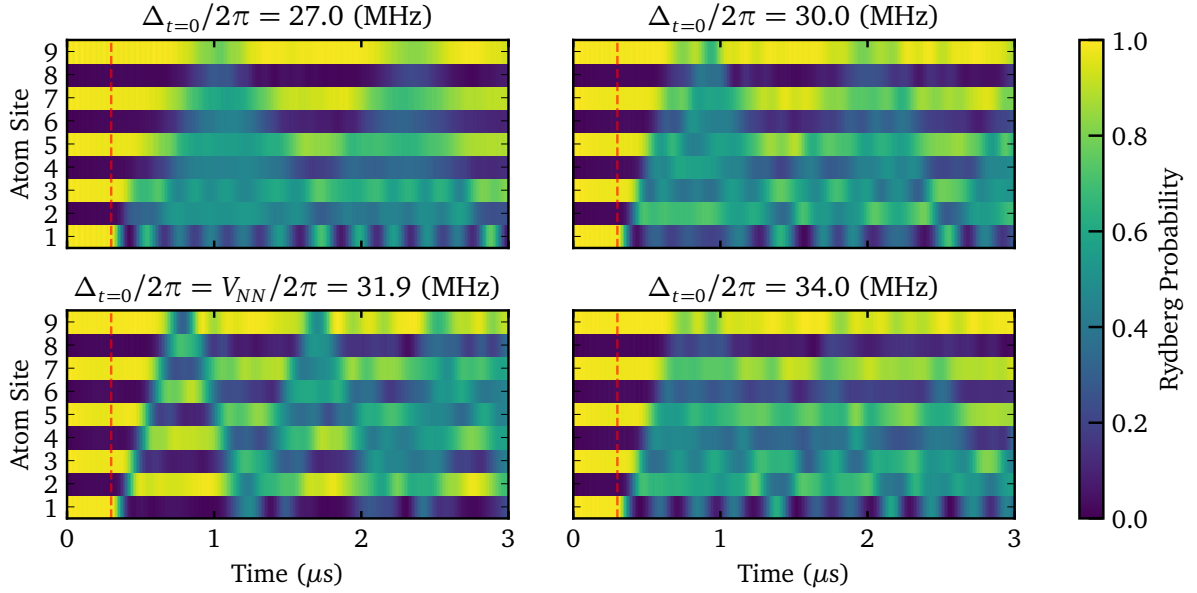**(a) Local quench protocol**
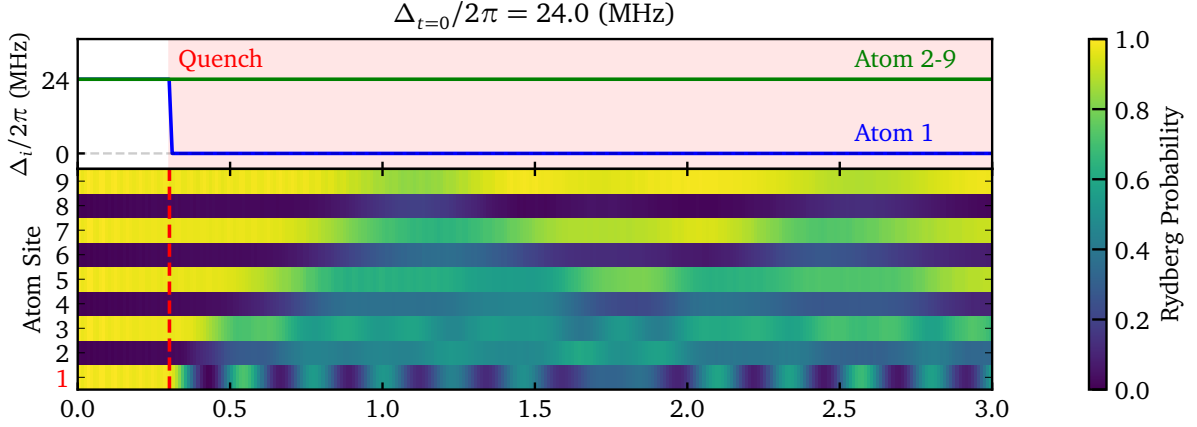
(b) Varying detuning

FIG. 11: Local quench edge atom At t = 0.00 μs system is in Z_2 ground state of Hamiltonian with $\Omega/2\pi = 4.00$ MHz, $a = 5.48$ μm $< R_B$ (strong nearest neighbour interactions). At t = 0.30 μs system is quenched by dropping detuning addressing atom site 1 to resonance over time step $dt = 0.01$ μs. Detuning addressing all other atoms is held constant at $\Delta_{t=0} = \Delta_{2-9}$. In **(a)** illustration of the single-site detuning regime is shown for $\Delta_{t=0}/2\pi = 24.0$ MHz but applies for all other detuning cases. In **(b)**, initial detuning is varied to see the effects on the post-quench dynamics. Initial detunings are chosen both within $\Delta_{t=0} < V_{NN}/2\pi$ and out of the blockade regime $\Delta_{t=0} \geq V_{NN}/2\pi$, ensuring that initial state ground state fidelity is over $> 95\%$ (see Figure 6). In all cases, a light cone emerges from quench site characterised by the linear delayed propagation.

To further study the behaviour, we look closely at the 9th atom's Rydberg state fidelity (see Figure 12). Deviations from perfect Rydberg fidelity of order 1%, are suggestive of a change at atom site 9 elicited by the quench at site 1. Therefore, by looking at the 9th atom closely, we can calculate the time it takes for the disruption at atom site 1 to be noted by the other end of the array and thus the speed in which information propagates throughout the system. In doing so, we take note of two observations. First, the propagation speed of information throughout the array is dependent on the blockade constraint with maximum speeds found for detunings near the anti-blockade boundary ($\Delta_{t=0} = V_{NN}$). Secondly, we observe the biggest fidelity changes in this same vicinity. In particular, on resonance with the NN interaction, $\Delta_{t=0} = V_{NN}$, the alteration in Rydberg fidelity is exaggerated compared to other detuning cases (minimum fidelity 23.1 % versus $\approx$ 70-80% for nearby detuning cases $\Delta/2\pi = 30.0, 34.0$ MHz). Additionally, the dip in fidelity is notably symmetric and localized. Overall, this behaviour is further suggestive that around NN interaction detuning there is a unique resonance associated with how information propagates throughout the array.

Furthermore, it is important to recognise that, despite the long range interactions of the system, the constrained light cone spreading of information throughout the array indicates a persistence of locality: changes at one end of the system do not instantaneously result in a change at the other end. This behaviour can be associated with the rapid decay of the interactions $\propto 1/R^6$ such that the system can be considered to have finite-range interactions. In Figure 12, it is shown that the NN approximation of th interaction describes the system almost identically.
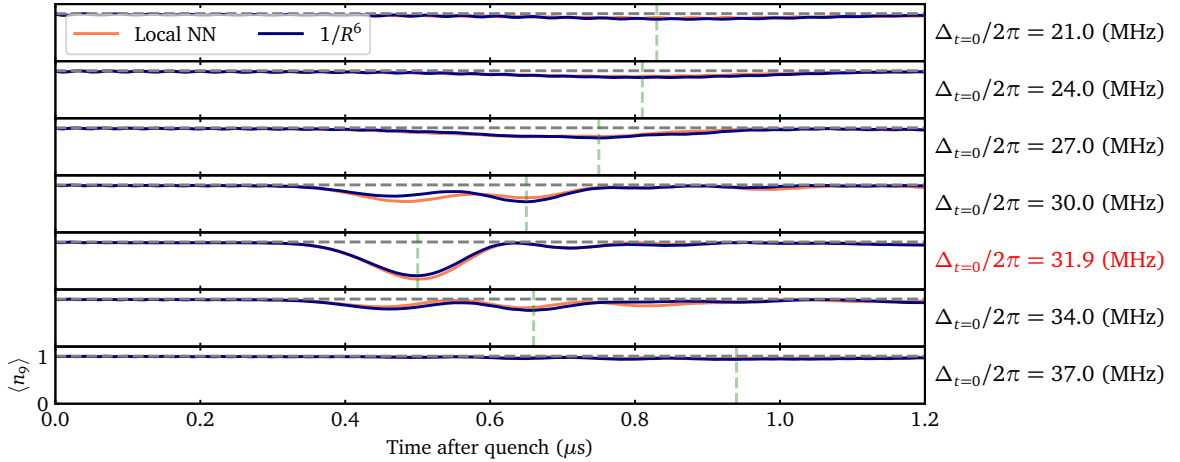

FIG. 12: Rydberg fidelities 9th atom Rydberg fidelity dynamics of atom at site i=9, following a quench at atom i=1, is studied to investigate the effect of propagation throughout the array. Quench regime follows that of Figure 11 with addition of initial detunings $\Delta_{t=0}/2\pi = 21.0, 37.0$ MHz to get a broader spectrum of the dynamics. Ninth atom Rydberg fidelity $\langle n_9 \rangle$ is initially at 1.00 (100%) as state starts out in Z_2 state with edge Rydberg excitations. The delayed drop in fidelity signifies arrival of information from the quench and is indicative of the locality of the system. Nearest neighbour detuning case, $\Delta_{t=0}=V_{NN}$, is highlighted for its unique resonant behaviour (deep localised well at $t \approx 0.5$ μs). The green dashed line indicates fidelity minimum for each case and is used to compare information propagation speeds. Nearest neighbour interaction model, $V_{ij} = V_{NN}\delta_{i,j\pm1}$, shown by the orange line to demonstrate the Rydberg array can be well described by a local nearest neighbour interaction model.

2. Entanglement entropy propagation

To investigate the light cone behaviour further, we look at the growth of entanglement entropy (EE) throughout the array. Given the nature of the quench, probing the half-chain EE, as conducted in the instance of the global quench (see Figure 10), does not provide a full insight into the spreading of entanglement. Instead, we look at how the single-site EE evolves following the quench (see Figure 13). We compare our results to the results of an unquenched array.
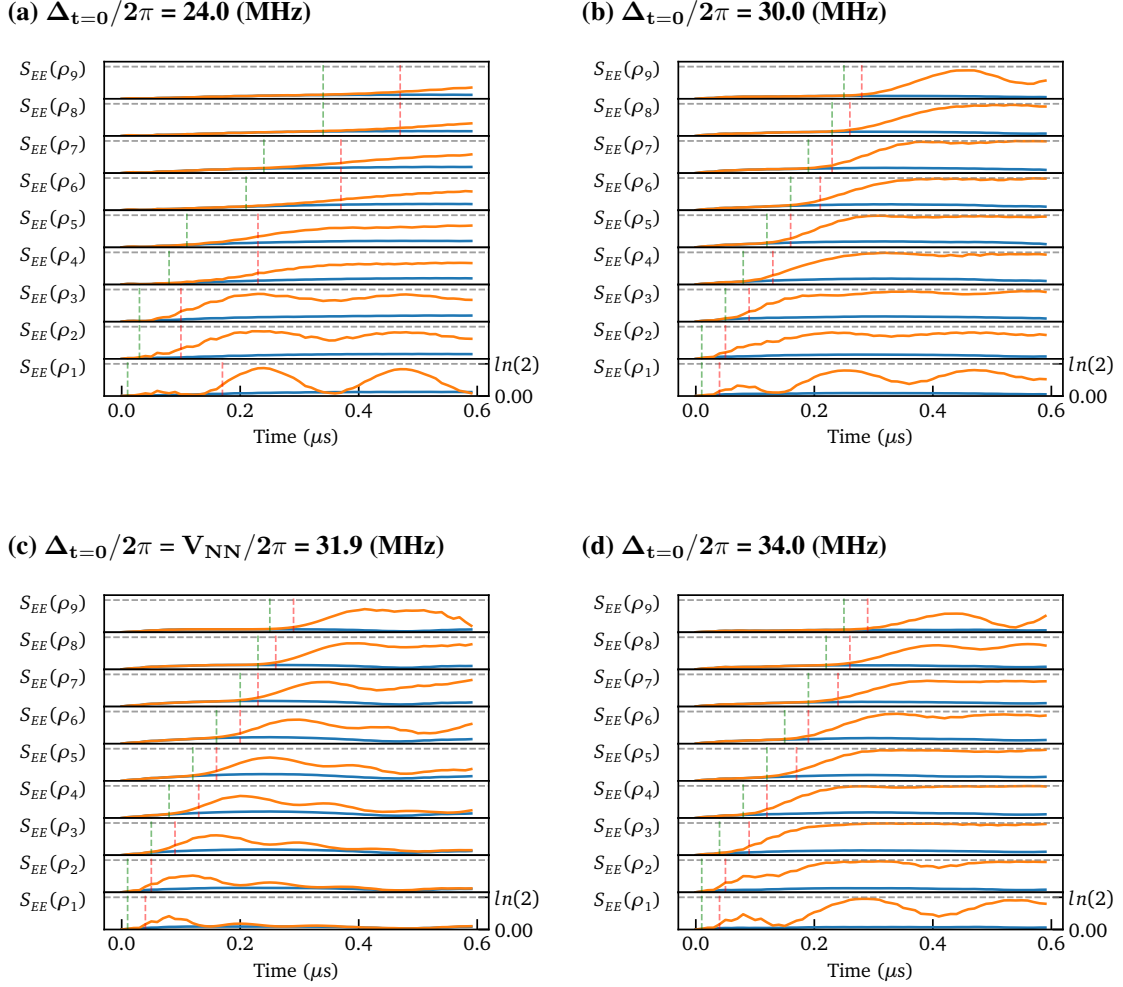

(a) $\Delta_{t=0}/2\pi = 24.0$ **(MHz)**

(b) $\Delta_{t=0}/2\pi = 30.0$ **(MHz)**

(c) $\Delta_{t=0}/2\pi = V_{NN}/2\pi = 31.9$ **(MHz)**

(d) $\Delta_{t=0}/2\pi = 34.0$ **(MHz)**

FIG. 13: EE propagation: local quench vs no quench Indicated by the *orange lines*, the individual site von Neumann entropy, $S(\rho_i) = -tr[\rho_i ln(\rho_i)]$, is calculated for atoms 1-9 following a local quench at atom site i=1, t = 0.00 μs for detunings studied in Figure 11. The *blue lines* illustrate EE for the unquenched system held at $\Delta_{const} = \Delta_{t=0}$. The distinction is used to quantify the EE on each atom site that is a result of the localised quench and not the background entangling of atoms in the array. The green dashed line indicates the timestamp where the quenched case EE, $S_{EE}(\rho_{quench})$, is 10% greater than the unquenched case $S_{EE}(\rho_{const})$. The red dashed line indicates the timestamps where the quench EE, $S_{EE}(\rho_{quench})$, is three standard deviations, 3σ, greater that the time averaged EE of the unquenched case $\langle S_{EE}(\rho_{const}) \rangle_{t<0.6\mu s}$. See Figure 14 for further analysis.
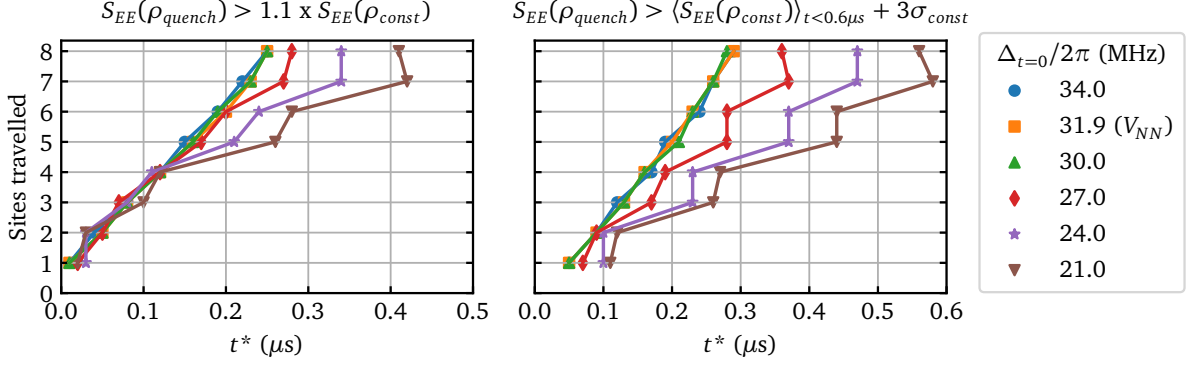
FIG. 14: EE propagation speeds Following results in Figure 13 (red and green dashed lines) the threshold EE arrival timestamps $t*$ are plotted against distance travelled along the array to gain an insight into the linearity and speed of the EE propagation. Two separate thresholds are used to account for the uncertainty in quantifying the arrival of the impulse. Moreover, EE at quench site 1 is ignored due to initial symmetry (qubit's 1 and 2 entangle at the same time). Addition of detuning cases $\Delta_{t=0}/2\pi$ = 21.0, 27.0 MHz included to further clarify the blockade detuning behaviour. In both threshold cases, it is clear the linearity in EE propagation breaks down for lower detuning cases, 21.0 MHz $\leq \Delta_{t=0}/2\pi \leq 27.0$ MHz with pairwise behaviour emerging (sequentially pairs of qubit entangling that the same time). For the higher detuning cases, approaching and going into the anti-blockade region, $\Delta_{t=0}/2\pi \geq 30.0$ MHz, entanglement propagation is linear with speed ≈ 30 sites/μs.

This allows us to identify the increase in entanglement throughout the array which is associated with the quench at atom site 1 and not the background entangling between atoms.

In all detuning cases, we again observe a lightcone-like wavefront following the shape of the changing Rydberg fidelities. This suggests that propagation of information throughout the system can be associated with a propagation of EE.

However, the linearised light cone picture is not exact for all cases. For example, for the $\Delta_{t=0}$ = 24.0 MHz case, the EE impulse for each subsequent pair of qubits appears to arrives in unison, straying away from linear propagation. This is observed in Figure 13a by the pairwise grouping threshold timestamps. The behaviour is further illustrated in Figure 14, where for all strongly blockaded detuning cases, $\Delta_{t=0}$ = 21.0 - 27.0 MHz, the propagation of EE is not uniform but bunches in pairs. In contrast, as detuning approaches the anti-blockade condition, EE entropy propagates linearly throughout the array at a faster uniform speed of ≈ 30 sites/μs, reflecting the faster propagation of information observed around the antiblockade boundary in Figure 12.

Furthermore, in Figure 13c, we observe unique resonant behaviour associated with the NN interaction detuning quench. This is manifested by formation of single-site EE entropy peaks which emerges sequentially throughout the array, contrasting the general steady growth and saturation of single-site EE for the other detuning cases.

3. Further insight: Concurrence

To further quantify the EE entropy results, we introduce another measurement of entanglement on the system: the concurrence. The concurrence gives a measure of how localised entanglement is around a pair of qubits. In the Figure 15, a colormap of the concurrence between NN qubit pairs, $C(i, i+1)$, is plotted along the array for the varying initial detunings both within the blockade and antiblockade regions to further investigate how entanglement emerges across the array following the quench.
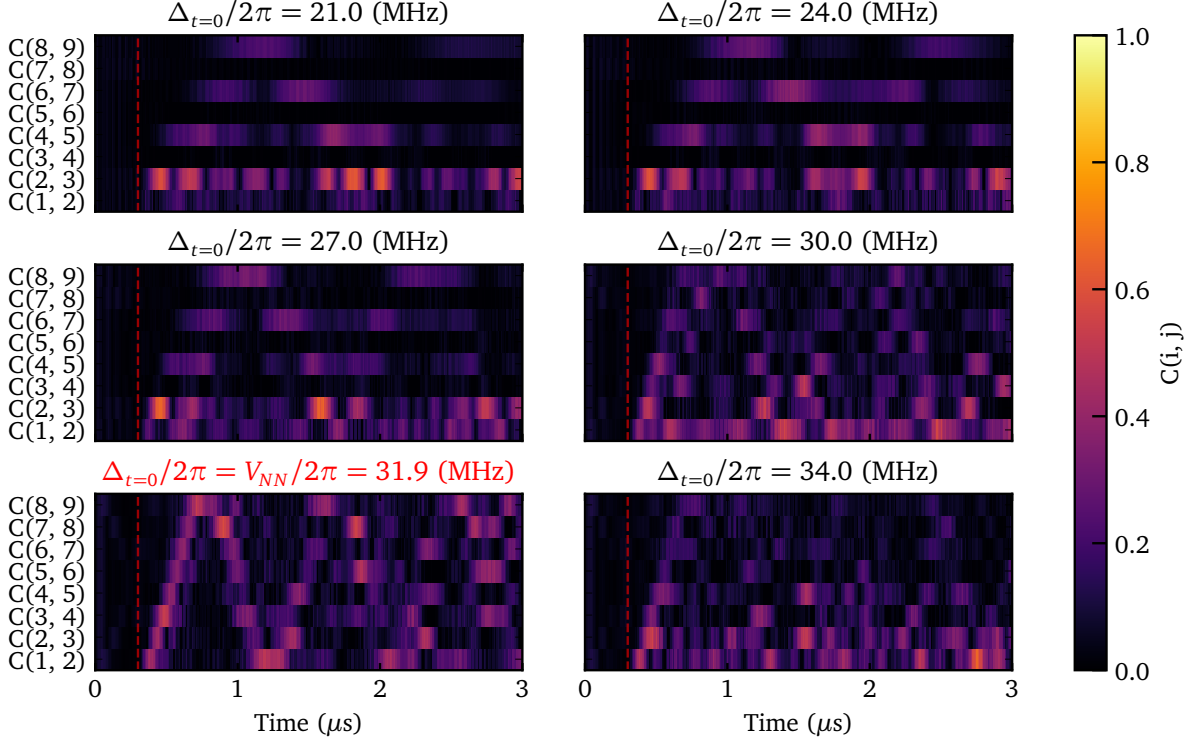

FIG. 15: Pairwise concurrence Concurrence dynamics between sequential pairs of the array following quench at $t = 0.30$ μs (quench routine performed in Figure 11) is studied to investigate pairwise qubit entanglement that can't be measured by EE partitions of the system. Range is between $C(i, j) = 0.00$ for a separable state and and $C(i, j) = 1.00$ for maximally entangled two qubit Bell states. Concurrence between other pairwise combinations of the array found to be ≈ 0.00, revealing the locality of the pairwise two qubit entanglement. For more details on concurrence see 'Entanglement measures' section. The resonant antiblockade detuning, $\Delta_{t=0} = V_{NN}$ is highlighted due to the compact jets of concurrence that emerge from the quench site. Behaviour appears quasiparticle like. On the other hand, at lower blockaded detunings, 21.0 MHz $\leq \Delta_{t=0}/2\pi \leq 27.0$ MHz, the concurrence is solely concentrated amongst sequential pairs (i & j = 2 & 3, 4 & 5, 6 & 7, 8 & 9) of the unquenched section of the array.

From our results, we highlight the NN interaction detuning case, $\Delta_{t=0} = V_{NN}$ where remarkably a jet of concurrence is observed propagating from the local quench site, reflecting on each end before eventually diffusing into the system at $t \approx 1.50$ μs. This ballistic propagation is particle-like, strongly suggesting a quasiparticle description of the post-quench behavior. Such

a description could further account for the compact wavefront observed in both the Rydberg fidelity and entanglement entropy results. Since concurrence measures pairwise entanglement, this result suggests that the initial quasiparticle behaviour is associated with an entangled qubit pair created at the quench site. Delving into this we looked at the Bell state fidelities of pairs of atom following the quench, but found no noteworthy results. Consequently, the nature of this quasiparticle behaviour warrants further studies.

Furthermore, our results confirm the strong pairwise entangling behaviour present at lower blockade detunings. This is reflected by the concurrence being concentrated amongst sequential pairs of the unquenched 8 atom array for all lower detuning cases. For example, the concurrence of atoms 6 & 7 and 8 & 9 is non-zero where as for atoms 7 & 8 the concurrence is strictly zero. This behaviour suggests that entanglement is localised to pairs of qubits throughout the array. The specific origin of the behaviour is unknown, but it is reasonable to assume that it has something to do with the blockade of the $|rr\rangle$ state.

B. Other localised quenches

The results of the singular edge atom quench reveal that the way in which information and entanglement propagate throughout the array is dependent on the strength of the blockade constraint. To extend the analysis, we highlight two more cases of locally quenching the array: quench of the centre atom and quench of the two edge atoms. For each case we study the single site Rydberg fidelity results and the pairwise concurrence results.

Quenching the centre atom results in a light cone spreading of information and entanglement throughout the array (see Figure 16a). Unlike the edge atom quench, the centre atom quench reveals a symmetry in this behaviour as the spreading propagates in both directions. Despite this difference, we still observe sequential pairwise concurrence behaviour associated with blockaded detuning and quasiparticle behaviour associated with resonant anti-blockade detuning $\Delta_{t=0} = V_{NN}$. Interestingly, in the later case, as the concurrence jets reflect off each end and recombine ($t \approx 0.65$ μs), they cancel each other out before reemerging on the other side. This observation, doesn't explicitly indicate the entanglement vanishing at this point but rather that the entanglement is no longer significantly confined to a pair - it could be mutlipartite. This behaviour is reflected in the second quench case (see Figure 16b) where around $t \approx 0.35$ μs the concurrence jets combine and cancel each other out.

Overall, both additional quenches cases support the characteristic behaviour observed in our initial quench case (single edge atom). Mainly, that at resonant detuning, $\Delta_{t=0} = V_{NN}$, we observe quasiparticle behaviour in the way in which information and entanglement propagates throughout the array. In addition to this, both quench cases reveal interesting behaviour associated with the two quasiparticle jets of concurrence combing with one another and canceling each other out. The nature of this is put forth as further study.
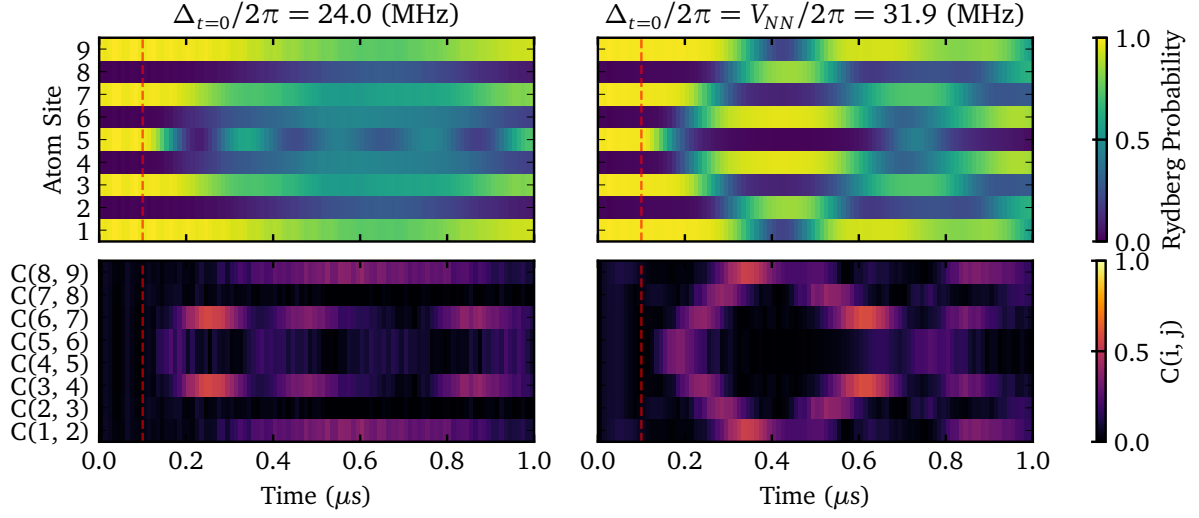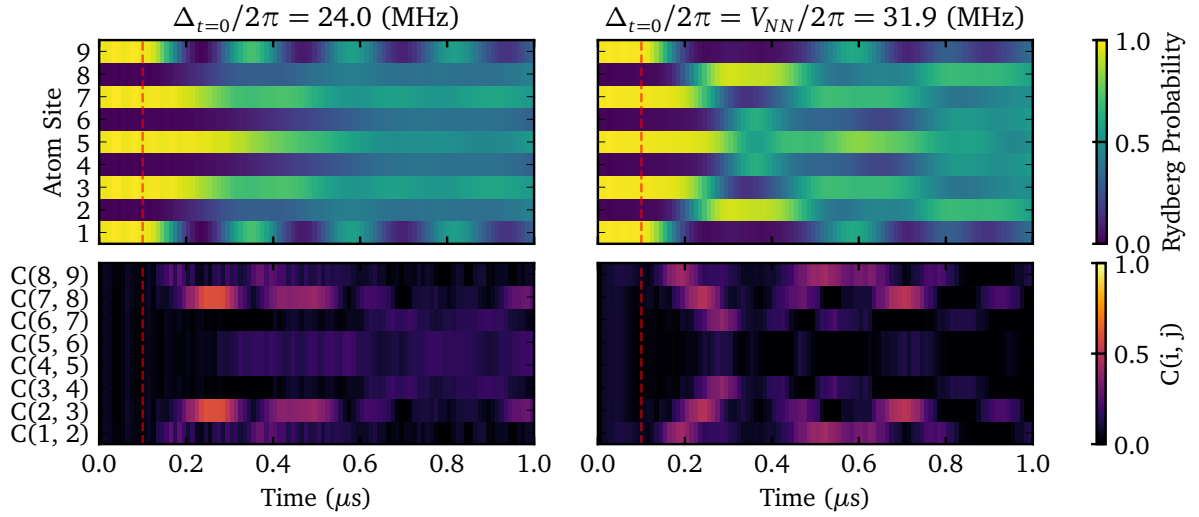
(a) Centre atom

(b) Edge atoms

FIG. 16: Other Local quenches Single-site Rydberg fidelity and pairwise concurrence dynamics following local quenches of centre atom **(a)** and both edge atoms **(b)** at $t = 0.10$ μs. Prequench state is Z_2 state with $a = 5.48$ μm $< R_B$ and $\Omega/2\pi = 4.00$ MHz (same initial configuration as Figure 11). Two detuning cases considered: $\Delta_{t=0}/2\pi = 24.0$ MHz (blockade) and $\Delta_{t=0}/2\pi = V_{NN}/2\pi = 31.9$ MHz (resonant antiblockade) to determine weather characteristic behaviour observed in singular edge atom quench is apparent in these quenches.

C. Outlook

Overall, we find that locally quenching the array opens up numerous opportunities to study rich quantum transport dynamics inaccessible to the case of the global quench. In studying these dynamics, we make two key observations:

1. Both quantum information and entanglement propagate from the quench site in a constrained light cone.

2. The dynamics of this propagation is very sensitive to the laser detuning and thus the constraining of the system. In particular, we observe resonant quasiparticle behaviour associated with locally quenching at the anti-blockade condition, $\Delta = V_{NN}$.

The first observation is a product of the rapid decay of van der Waals interaction, resulting in a finite range interactions and thus locality. This behaviour is well documented in multiple experimental and numerical studies of similar quantum Ising-type models [21–23] and has many exciting applications. Notably, with Rydberg atom arrays proving as worthy candidates for both digital and analogue quantum computing [24], investigating the timescales of information and EE propagation throughout the array could lead to additional insights into the speed in which errors propagate. Moreover, the strongly, locally correlated nature of the system could enable quantum communication protocols [25]. In particular, at resonant anti-blockade condition ($\Delta_{t=0} = V_{NN}$) where information is efficiently and compactly propagated throughout the array.

From the second observation we open up questions surrounding EE dynamics. It has been strongly suggested that the growth and spreading of EE within an isolated quantum many-body system can give insights into the mechanisms behind quantum phase transitions and quantum thermalisation [26, 27]. Accordingly, there has been a push to describe EE transport phenomena with the support of a quasiparticle picture [28, 29]. Recognising such behaviour in our experimentally accessible system could open up further studies. Moreover, by recognising regions where entanglement is pairwise, such as in strongly blockaded regions ($\Delta_{t=0} << V_{NN}$), we could introduce ways of simplifying the dynamics system. For example, a pairwise quantum dimer model which has been used in quantum spin liquids [30] and was suggested by Ref. [7] to try explain scar behaviour following the global quench.

To extend our analysis of the local quench outside of this report, it would be useful to get a more direct, quantitative comparison of the Rydberg fidelity results with the entanglement entropy/concurrence results. Overlaying and comparing the single-site results of both measures would enable us to delve deeper into how the sequential change of fidelities throughout the array can be associated with the spreading of entanglement entropy.

6.   CONCLUSION

Overall, we demonstrate through both global and local quenches, that the Rydberg atom array unveils numerous opportunities for studying rich out-of-equilibrium dynamics associated with closed quantum many-body systems.

By globally quenching the array, we investigate the surprising, non-trivial behaviour of quantum many-body scars. We find that this behaviour is associated with ordered eigenenergy spreading of the state vector and slow entanglement entropy growth following the quench of the Z_2 state. In doing so, we showcase significant results associated with studying the solution space of the Rydberg interaction Hamiltonian Eq. (7) as opposed to the PXP Hamiltonian in which most studies of the scar behaviour have been focused [8].

On the other hand, by locally quenching the Z_2 state of the system, we find compelling quantum transport phenomena associated with the light cone spreading of information and entanglement entropy from the quench site. Specifically, we find that the strength of the blockade constraint has a significant impact on these dynamics. In a system with strong blockade, we find that entanglement entropy does not propagate linearly throughout the array and instead forms sequentially on pairs of qubits. As we surpass the blockade constraint and enter antiblockade, this behaviour breaks down and linear propagation is observed. In particular, when we quench on resonance with the anti-blockade condition, we observe quasiparticle-like behaviour in the way entanglement and concurrence propagate throughout the array. The underlying nature of these results is uncertain and warrants further study. However, the results themselves motivate the development of a generalised description of how entanglement entropy propagates throughout the system and thus how statistical mechanics can emerge from quantum mechanics [4].

Of course, our work was limited by the computational speeds of a laptop, highlighting itself the need for quantum simulators. Nonetheless, by using concepts in quantum information theory, we hope to demonstrate that even at scales below 10 qubits a lot of compelling quantum dynamics emerge. In a way, we conclude by celebrating quantum mechanics's remarkable ability to find order in situations where things should appear disordered.

7.   ACKNOWLEDGEMENTS

[1] Griffiths, D. J., & Schroeter, D. F. *Introduction to Quantum Mechanics* (3rd ed.). Cambridge: Cambridge University Press. (2018). https://doi.org/10.1017/9781316995433

[2] Ott, E. *Chaos in Dynamical Systems*. 2nd edn. Cambridge: Cambridge University Press. (2002). https://doi.org/10.1017/CBO9780511803260

[3] Neill, C., Roushan, P., Fang, M. *et al.* Ergodic dynamics and thermalization in an isolated quantum system. *Nature Phys* 12, 1037–1041 (2016). https://doi.org/10.1038/nphys3830

[4] Calabrese, P. Entanglement and thermodynamics in non-equilibrium isolated quantum systems. *Physica A: Statistical Mechanics and Its Applications*, 504, 31-44. (2018). https://doi.org/10.1016/j.physa.2017.10.011

[5] Fraxanet, J., Salamon, T., & Lewenstein, M. The Coming Decades of Quantum Simulation. In *Lecture Notes in Physics* (pp. 85–125). Springer International Publishing. (2023). https://doi.org/10.1007/978-3-031-32469-7

[6] Adams, Charles, and Nikola Šibalić. Rydberg Physics. IOP Publishing Limited. (2018). https://dx.doi.org/10.1088/978-0-7503-1635-4

[7] Bernien, H., Schwartz, S., Keesling, A. *et al.* Probing many-body dynamics on a 51-atom quantum simulator. *Nature* 551, 579–584. (2017). https://doi.org/10.1038/nature24622

[8] Serbyn, M., Abanin, D.A. & Papić, Z. Quantum many-body scars and weak breaking of ergodicity. *Nat. Phys.* 17, 675–685. (2021). https://doi.org/10.1038/s41567-021-01230-2

[9] Schauss, P. Quantum simulation of transverse Ising models with Rydberg atoms. *Quantum Sci. Technol.* 3, 023001. (2018). https://doi.org/10.1088/2058-9565/aa9c59

[10] Mbeng, G. B., Russomanno, A., Santoro, G. E. The quantum Ising chain for beginners. arXiv:2009.09208. (2020). https://doi.org/10.48550/arXiv.2009.09208

[11] QuEra Computing. Bloqade.jl documentation. Retrieved 04/04/2024, from https://queracomputing.github.io/Bloqade.jl/stable/

[12] Hatano, N., Suzuki, M. Finding Exponential Product Formulas of Higher Orders. In: Quantum Annealing and Other Optimization Methods. Lecture Notes in Physics, vol 679. Springer, Berlin, Heidelberg. Pages 37-68. (2005). https://doi.org/10.1007/11526216

[13] Sachdev, S. Quantum Phase Transitions. Cambridge University Press. (2011). https://doi.org/10.1017/CBO9780511973765

[14] Nielsen, M. A., and Chuang, I. L. Quantum Computation and Quantum Information: 10th Anniversary Edition. Cambridge University Press. (2010). https://doi.org/10.1017/CBO9780511976667

[15] Wootters, William K. "Entanglement of Formation of an Arbitrary State of Two Qubits." *Physical Review Letters* 80, Iss. 10, 2245–2248 (1998). https://doi.org/10.1103/PhysRevLett.80.2245

[16] Turner, C.J., Michailidis, A.A., Abanin, D.A. *et al.* Weak ergodicity breaking from quantum many-body scars. *Nature Phys* 14, 745–749 (2018). https://doi.org/10.1038/s41567-018-0137-5

[17] Bluvstein, D., Omran, A. Levine, H.*et al.*, Controlling quantum many-body dynamics in driven Rydberg atom arrays. *Science* 371, 1355-1359. (2021). https://doi.org/10.1126/science.abg2530

[18] Yoshii, Ryosuke, Shion Yamashika, and Shunji Tsuchiya. Entanglement Propagation in Thermalization of an Isolated Quantum System. arXiv:2003.10106 (2022). https://doi.org/10.48550/arXiv.2003.10106

[19] Eisert, J., Cramer, M., and Plenio, M. B. Colloquium: Area Laws for the Entanglement Entropy. American Physical Society (APS). *Reviews of Modern Physics*, vol 82, no. 1, pp. 277–306. (2010). https://doi.org/10.1103/RevModPhys.82.277

[20] Nandkishore, R., & Huse, D. A. Many-Body Localization and Thermalization in Quantum Statistical Mechanics. *Annual Review of Condensed Matter Physics*, 6, 15-38. (2015). https://doi.org/10.1146/annurev-conmatphys-031214-014726

[21] Jurcevic, P., Lanyon, B., Hauke, P. et al. Quasiparticle engineering and entanglement propagation in a quantum many-body system. *Nature* 511, 202–205 (2014). https://doi.org/10.1038/nature13461

[22] Cheneau, M., Barmettler, P., Poletti, D. *et al*. Light-cone-like spreading of correlations in a quantum many-body system. *Nature* 481, 484–487 (2012). https://doi.org/10.1038/nature10748

[23] Schachenmayer, J. and Lanyon, B. P. and Roos, C. F. and Daley, A. J. Entanglement Growth in Quench Dynamics with Variable Range Interactions. *Phys. Rev. X*, Vol. 3. Iss. 3. (2013). https://doi.org/10.1103/PhysRevX.3.031015

[24] Kim, M., Ahn, J., Song, Y. et al. Quantum computing with Rydberg atom graphs. J. Korean Phys. Soc. 82, 827–840 (2023). https://doi.org/10.1007/s40042-023-00774-1

[25] Bose, S. Quantum communication through spin chain dynamics: an introductory overview. Contemp. Phys. 48, 13–30 (2007).https://doi.org/10.1080/00107510701342313

[26] Adam M. Kaufman *et al*. Quantum thermalization through entanglement in an isolated many-body system. *Science* 353, 794-800 (2016). https://doi.org/10.1126/science.aaf6725

[27] Zeng, B., Chen, X., Zhou, D.-L., & Wen, X.-G. (2018). Quantum Information Meets Quantum Matter – From Quantum Entanglement to Topological Phase in Many-Body Systems. *arXiv preprint arXiv:1508.02595*. https://doi.org/10.48550/arXiv.1508.02595

[28] Pasquale Calabrese and John Cardy. Evolution of entanglement entropy in one-dimensional systems. *J. Stat. Mech.* 2005, 04, P04010. (2005). https://dx.doi.org/10.1088/1742-5468/2005/04/P04010

[29] Vincenzo Alba & Pasquale Calabrese. (2017). Entanglement and thermodynamics after a quantum quench in integrable systems. *Proceedings of the National Academy of Sciences*, 114(30), 7947-7951. https://doi.org/10.1073/pnas.1703516114

[30] Lucile Savary and Leon Balents. Quantum spin liquids: A review. *Rep. Prog. Phys.* 80 016502. (2017). http://dx.doi.org/10.1088/0034-4885/80/1/016502

8.   SUMMARY FOR A GENERAL AUDIENCE

Using lasers, it is possible to cool atoms to near zero temperatures, trapping them in space. This remarkable technique allows one to create arrays of atoms fixed in place – a perfect workbench for studying quantum many-body mechanics. In this work, we carry out a computer simulation of the equations governing an array of such atoms addressed by perpendicular lasers, known as driving lasers. The driving lasers alter the energy state of the outer electron of each atom. Specifically, we can have the lasers send the electron to a high energy state known as the Rydberg state. In doing so, we encode information onto the array in the form of quantum bits, qubits, characterised by weather the electron is in the Rydberg state or not (our 'on'/'off').

Through this encoding, we can study what happens when the system is taken out of equilibrium. Analogous to a metal worker quenching a hot piece of iron in cold water, we quench our system by rapidly changing the frequency of the driving lasers. This results in a flurry of exciting non-equilibrium dynamics. Due to the strong interactions between high energy Rydberg states of the atoms, this out of equilibrium regime leads to a phenomenon know as quantum entanglement where information about the state of each atom becomes non-local and spreads out across the array. In our work, we focus on how constraints imposed by the driving laser and and atom array spacing, affect how entanglement forms and spreads across the system. Overall, we strive to demonstrate the potential of the Rydberg atom array as a platform for studying compelling out of equilibrium quantum behaviour.

A.   CODE

The dynamics of the system was coded up in python using libraries Numpy and Scipy. Plots where generate using Matplotlib. For access to the code visit github page: https://github.com/oliverlind/RydbergQubit

B.   DENSITY MATRICES

A finite dimensional quantum system can either be described by a pure or mixed states. Pure states give an exact description of the system encoded in the state vector $|\psi\rangle$. Mixed states, on the other hand, describe the system as a classical mixture of state vectors each with a corresponding probability p_i. This is a result of the uncertainty of the system's exact state. Crucially, this is not the same as quantum superposition. The uncertainty is purely classical.

To represent mixed states we use a density matrix which is defined as follows:

$$\rho = \sum_i^n p_i |\psi_i\rangle \langle\psi_i| .$$

The result is a statistical ensemble of the n pure states $|\psi_i\rangle$ that the system could be in, weighted by probabilities p_i. The outer product formulation is used to distinguish classical uncertainty from quantum superposition. If we had written ρ as a sum of state vectors $|\psi_i\rangle$, we would have got a quantum superposition. Instead, the outer product matrix formulation ensures there is no coherence between the potential state vectors $|\psi_i\rangle$ in the density matrix description ρ.